

CWISEP J193518.59–154620.3: An Extremely Cold Brown Dwarf in the Solar Neighborhood Discovered with CatWISE

FEDERICO MAROCCO,^{1,2,*} DAN CASELDEN,³ AARON M. MEISNER,^{4,†} J. DAVY KIRKPATRICK,² EDWARD L. WRIGHT,⁵ JACQUELINE K. FAHERTY,⁶ CHRISTOPHER R. GELINO,² PETER R. M. EISENHARDT,¹ JOHN W. FOWLER,⁷ MICHAEL C. CUSHING,⁸ ROC M. CUTRI,² NELSON GARCIA,² THOMAS H. JARRETT,⁹ RENATA KOONTZ,^{10,1} AMANDA MAINZER,¹ ELIJAH J. MARCHESE,^{10,1} BAHRAM MOBASHER,¹⁰ DAVID J. SCHLEGEL,¹¹ DANIEL STERN,¹ AND HARRY I. TEPLITZ²

¹*Jet Propulsion Laboratory, California Institute of Technology, 4800 Oak Grove Dr., Pasadena, CA 91109, USA*

²*IPAC, Mail Code 100-22, Caltech, 1200 E. California Blvd., Pasadena, CA 91125, USA*

³*Gigamon Applied Threat Research, 619 Western Avenue, Suite 200, Seattle, WA 98104, USA*

⁴*National Optical Astronomy Observatory, 950 N. Cherry Ave., Tucson, AZ 85719, USA*

⁵*Department of Physics and Astronomy, UCLA, 430 Portola Plaza, Box 951547, Los Angeles, CA 90095-1547, USA*

⁶*Department of Astrophysics, American Museum of Natural History, Central Park West at 79th Street, NY 10024, USA*

⁷*230 Pacific St., Apt. 205, Santa Monica, CA 90405, USA*

⁸*Department of Physics and Astronomy, University of Toledo, 2801 West Bancroft St., Toledo, OH 43606, USA*

⁹*Department of Astronomy, University of Cape Town, Private Bag X3, Rondebosch, 7701, South Africa*

¹⁰*University of California, Riverside, 900 University Ave, Riverside, CA 92521, USA*

¹¹*Lawrence Berkeley National Laboratory, Berkeley, CA 94720, USA*

(Received April 22, 2019; Revised June 11, 2019; Accepted June 24, 2019)

Submitted to ApJ

ABSTRACT

We present the discovery of an extremely cold, nearby brown dwarf in the solar neighborhood, found in the CatWISE catalog (Eisenhardt et al., in prep.). Photometric follow-up with *Spitzer* reveals that the object, CWISEP J193518.59–154620.3, has $\text{ch1} - \text{ch2} = 3.24 \pm 0.31$ mag, making it one of the reddest brown dwarfs known. Using the *Spitzer* photometry and the polynomial relations from Kirkpatrick et al. (2019) we estimate an effective temperature in the ~ 270 – 360 K range, and a distance estimate in the 5.6–10.9 pc range. We combined the *WISE*, *NEOWISE*, and *Spitzer* data to measure a proper motion of $\mu_\alpha \cos \delta = 337 \pm 69$ mas yr⁻¹, $\mu_\delta = -50 \pm 97$ mas yr⁻¹, which implies a relatively low tangential velocity in the range 7–22 km s⁻¹.

Keywords: brown dwarfs – infrared: stars – proper motions – solar neighborhood

1. INTRODUCTION

The census of objects in the solar neighborhood has been growing steadily in recent years (Henry et al. 2018). The advent of large-area optical and near-infrared surveys (e.g. 2MASS, Skrutskie et al. 2006; SDSS, York et al. 2000; UKIDSS, Lawrence et al. 2007; VHS, McMahon et al. 2013; PanSTARRS, Chambers et al. 2016; AllWISE, Cutri et al. 2013), and the recent *Gaia* sec-

ond data release (Gaia Collaboration et al. 2018), have given us the opportunity to identify previously overlooked members of the 20 pc sample.

Despite recent discoveries of nearby ultracool dwarfs (Scholz & Bell 2018; Faherty et al. 2018; Cushing et al. 2018; Mamajek et al. 2018), the census of the coldest, lowest mass constituents of the solar neighborhood remains largely incomplete. Kirkpatrick et al. (2019) found that the completeness limit for the T and Y dwarfs sample steeply declines as a function of effective temperature (T_{eff}), from 19 pc in the 900–1050 K interval, down to 8 pc in the 300–450 K interval. At even lower T_{eff} , only one object has been so far identified, WISE J085510.83–071442.5 (hereafter

Corresponding author: Federico Marocco
federico.marocco@jpl.nasa.gov

* NASA Postdoctoral Program Fellow

† Hubble Fellow

WISE J0855–0714, Luhman 2014), at a distance of 2.3 pc.

The paucity of objects in this temperature regime has prevented us from answering questions fundamental to astrophysics: how does star formation create objects of extremely low mass, and with what efficiency? Whereas the form of the mass function is well established for higher mass stars, it is far less constrained for the lowest mass stars and brown dwarfs. Objects of the lowest mass, including brown dwarfs, may, in fact, have several paths to creation depending upon their birth environment. Studies of star formation regions (e.g. Burgess et al. 2009) and nearby, young moving groups (Faherty et al. 2016; Best et al. 2017) have shown that objects as low-mass as a few Jupiter masses (M_{Jup}) can form in isolation. Older, isolated field objects with these masses therefore must exist, and will have had many Gyr to cool, making them cold analogs to planets in exosolar systems. Although establishing the diversity of low-mass star formation from cluster to cluster is important, observing more of these frigid, free-floating objects in the well-mixed field population will enable us to determine the frequency with which low-mass objects are formed across the age of the Galaxy.

Preliminary results from Kirkpatrick et al. (2019) show that the cutoff mass for star formation, if there is one, must be lower than $10 M_{\text{Jup}}$ since the model predictions assuming such a cutoff are already underpredicting the number of objects found. In order to test cutoffs of lower mass, we require more objects of extremely low temperature, akin to WISE J0855–0714.

As its name suggests, WISE J0855–0714 was discovered using data from *WISE* (Wright et al. 2010), whose *W1* (3.4 μm) and *W2* (4.6 μm) bands are ideally placed to identify extremely cold brown dwarfs with their red *W1* – *W2* colors (in contrast to the blue *W1* – *W2* colors of stars) because the *W2* band measures the peak of the spectral energy distribution while the *W1* band lies in a region of strong methane absorption (Burrows et al. 1997). WISE J0855–0714 is relatively bright in *W2* (13.89 ± 0.05 mag, Luhman 2014), and so, despite the “statistics of one”, Wright et al. (2014) estimated the 68% confidence range for the number of “0855-like” objects in the existing AllWISE dataset to be 4–35, with a median of 15.

Finding more of these hidden solar neighbors is one of the goals of CatWISE, a NASA Astrophysics Data Analysis Program (ADAP) funded project combining data from the 2010 to 2016 phases of the *WISE* mission, to generate an all-sky photometric and astrometric catalog (Eisenhardt et al., in prep.).

Here we present CWISEP J193518.59–154620.3 (hereafter CWISEP J1935–1546), an extremely cold brown dwarf at ~ 8 pc discovered in the preliminary CatWISE catalog¹. Its *W1* – *W2* color, and follow-up *Spitzer* photometry, suggest CWISEP J1935–1546 has an effective temperature comparable to that of WISE J0855–0714, in the 270–360 K range, making it one of the coldest brown dwarfs identified so far.

In Section 2, we briefly describe the CatWISE data processing and the preliminary catalog content; Section 3 details the machine-learning-based procedure used to identify CWISEP J1935–1546; in Section 4 we present our *Spitzer* follow-up photometry, and in Section 5 we combine the *Spitzer* data with the *WISE* data to refine the motion measurement for this target. Finally, in Section 6 we derive the basic properties for this cold new member of the solar neighborhood.

2. CATWISE

CatWISE is an infrared photometric and astrometric catalog consisting of 900,849,014 sources over the entire sky selected from *WISE* and *NEOWISE* data collected from 2010 to 2016 at *W1* and *W2*.

CatWISE adapted the AllWISE pipeline to work on the coadded *WISE* and *NEOWISE* images provided by unWISE (Meisner et al. 2018a,b). A full description of CatWISE is provided in Eisenhardt et al. (in prep.), and of the AllWISE pipeline in Cutri et al. (2013) and Kirkpatrick et al. (2014). Here we summarize the steps relevant to the discovery of CWISEP J1935–1546.

Source detection for the preliminary CatWISE catalog was performed using MDET (Marsh & Jarrett 2012), which works simultaneously in *W1* and *W2*. The full-depth unWISE coadds (Meisner et al. 2018b) were resampled from 2048×2048 (2.75"/pixel) format to the 4095×4095 (1.375"/pixel) format used by MDET for *WISE* source detection, using the Image Co-addition with Optional Resolution Enhancement software (ICORE, Masci 2013), and an appropriate point spread function (PSF). The PSF interpolation kernel smooths the images, providing a matched filter for optimal detection of isolated point sources. The “std” unWISE images were used for uncertainties, as these provide the standard deviation at each coadd pixel of the individual *WISE* exposures. The detection threshold was set at $\text{SNR} = 1.8$, yielding a differential source reliability of 50% based on deeper *Spitzer* data from the S-COSMOS program (Sanders et al. 2007).

¹ CWISEP is the official designation for sources identified in the CatWISE Preliminary catalog, see Eisenhardt et al., in prep.

The WPHOT software package developed for the AllWISE pipeline (Cutri et al. 2013), was adapted to perform source photometry and astrometry for CatWISE. Two main changes are worth highlighting here:

(1) For AllWISE, WPHOT propagates each source position detected by MDET in the coadded images to individual exposures, solving for the least-square best-fit to the PSF, to determine source position and fluxes (hereafter “stationary fit”). An alternative fit is also performed, allowing for linear motion of the source through the individual exposures (hereafter “motion fit”). This solution provides, along with motion, an alternative measurement of position, propagated to a chosen reference epoch, as well as fluxes.

For a given inertial position in each sky coverage, the ~ 12 exposures which are combined in each unWISE epoch coadd (Meisner et al. 2018a) are obtained within less than two days. As a result, the position of sources beyond the solar system can be assumed to be fixed for each epoch. Therefore CatWISE used unWISE epoch coadd images in place of individual exposures when running WPHOT.

(2) The other significant modification to the AllWISE version of WPHOT involves the treatment of the PSF asymmetry. The WISE PSF is asymmetric with respect to the scanning direction (which is along lines of ecliptic longitude). The scan direction is similar for all individual images in an epoch coadd, and a given inertial position is scanned in opposite directions every six months, i.e. in consecutive epochs (except very near an ecliptic pole). Since WPHOT was not designed to use a time-dependent PSF, CatWISE chose to measure source properties separately for the (typically four or more) epoch coadds in each of the two scan directions, and then merge the two results.

The Preliminary CatWISE Catalog is available at catwise.github.io, and will soon be available on the NASA/IPAC Infrared Science Archive² as well. From comparison to *Spitzer*, the signal-to-noise-ratio = 5 Vega magnitude limits are $W1 = 17.58$ mag and $W2 = 16.43$ mag (cf. $W1 = 16.90$ mag and $W2 = 15.95$ mag for AllWISE). From comparison to *Gaia* DR2 (Lindgren et al. 2018), CatWISE measures motions to a 1σ accuracy of 100 mas yr^{-1} for sources ~ 3 mag fainter than those measured with a similar accuracy in AllWISE, and achieves motion measurement accuracy that is 10 times better at $W2 = 15$ mag (Eisenhardt et al., in prep.), as expected given the longer time baseline afforded by the combined data.

² <https://irsa.ipac.caltech.edu/>

3. TARGET SELECTION

CWISEP J1935–1546 was found as part of our larger effort to identify and characterize very cold brown dwarfs using CatWISE. The search was conducted using the PYTHON package *XGBoost*³ (Chen & Guestrin 2016), which implements machine learning algorithms under the gradient boosting framework.

In general applications of supervised learning with *XGBoost*, one trains and evaluates an *XGBoost* model with a set of previously classified samples. This ground truth dataset is used throughout the development process to find a model with effective features and hyperparameters. Our application followed this general supervised learning paradigm.

We evaluated multiple *XGBoost* classifiers in target selection. CWISEP J1935–1546 was selected by our classifier that targets faint and red objects. More specifically, the classifier is restricted to training with and classifying point sources with $W2 > 14$ mag and $W1 - W2 > 1$ mag, or within 3σ of those limits, therefore consistent with T or Y spectral type (see e.g. Kirkpatrick et al. 2011).

To build our training set, since the prevalence of our target class (herein “positive”) is so low, and our compensatory sample weights for the remainder of the data set (herein “negative”) are also low by consequence, we manually classified samples for the positive class versus randomly sampled for the negative class. We took confirmed objects from the literature, and motion-confirmed objects from our candidate lists, and cross-matched them against CatWISE to obtain their CatWISE data. We removed/corrected mismatches until we were confident that the remaining training set held an insignificant number of mismatched training objects. This set, consisting of ≈ 200 objects, became our positive class.

We carefully selected sample weights to achieve robust classification. Firstly, we weighted samples of the positive and negative class as the inverse proportion of the total number of objects in each class within the training data. Consequently, samples belonging to the low population positive class received higher weight, and those belonging to the high population negative class received lower weight, so that

$$\sum_{i=0}^{n_{neg}} w_{neg,i} = \sum_{i=0}^{n_{pos}} w_{pos,i} \quad (1)$$

where $w_{neg,i}$, $w_{pos,i}$ are the weight for a single member of the negative and positive class, respectively, and n_{neg} ,

³ <https://xgboost.readthedocs.io/en/latest/>

n_{pos} are the total number of objects in the negative and positive class.

Next, we distributed weights within the positive class by $W2$ magnitude, creating an even distribution of total weights per given 0.5 bin of $W2$ magnitude. That is, our training data contained fewer faint $W2$ magnitude positive class members, so their weights were proportionally higher than bright $W2$ magnitude positive class members. In practice

$$\sum_{i=0}^{n_{pos,W2}} w_{pos,W2,i} = \sum_{i=0}^{n_{pos,W2+0.5}} w_{pos,W2+0.5,i} \quad (2)$$

where $w_{pos,W2,i}$, $w_{pos,W2+0.5,i}$ are the weight for a single member of the positive class in a given 0.5 magnitude bin (e.g. $14.5 \leq W2 < 15.0$ mag) and in the adjacent magnitude bin, respectively, while $n_{pos,W2}$, $n_{pos,W2+0.5}$ are the total number of objects in the two bins in question.

Machine-learning classifiers are defined by two different sets of parameters – model parameters and hyperparameters (also referred to as tuning parameters). Model parameters are estimated by the machine learning algorithm itself, from the data, as part of the learning process. Hyperparameters on the other hand cannot be estimated directly from the data, as they regulate the learning process itself (see e.g. Kuhn & Johnson 2013). Examples of hyperparameters are the k in k -nearest neighbor interpolation, or the learning rate for training. Finding the optimal set of hyperparameters is itself a complex problem, and several approaches have been adopted (see Claesen & De Moor 2015, and references therein).

We searched with *Scikit-learn*'s randomized cross-validation function for optimized hyperparameters (*RandomizedSearchCV*; Pedregosa et al. 2011). The function takes in a model, the training set, a selection of hyperparameters, and distributions from which to draw their guesses. It then picks hyperparameter values from the provided distributions, and trains and tests the model, searching for the values that optimize the model performance. However, experimentally we found that a low learning rate of 0.0135, manually enforced outside of the parameter search, lead to the greatest reduction of the classification error rate. The classification error rate is defined as n_{wrong}/n_{tot} , where n_{wrong} is the number of misclassified objects, and n_{tot} is the total number of classified objects (see e.g. Tan 2018, Chapter 4.2).

After first training each *XGBoost* classifier with our initial training set, we applied it to the entire CatWISE catalog, and selected the objects (usually between 10,000 and 25,000) with the highest predicted proba-

bility membership in the positive class. We then visually inspected each object, using available optical, near- and mid-infrared images (taken from DSS, 2MASS, UKIDSS, PanSTARRS, and AllWISE) and the online image blinking/visualization tool WiseView⁴ (Caselden et al. 2018). Objects confirmed to be real, with $W1-W2$ color visually consistent with $W1 - W2 > 1$ mag, and with visible motion (confirming they are nearby), were added to the positive class. Common false positives included objects that were found to be unflagged artifacts, variable sources leading to spurious motion measurements, and partly blended objects with contaminated photometry and/or astrometry.

We then iterated by re-training the classifier on the full training data, and applied the re-trained classifier to the entire catalog to select another batch of high probability positive class entries. Periodically, we would validate both the manually labelled and randomly sampled training data to remove mislabelled objects. We would do this by performing various train-test splits and visually inspecting negatively labelled entries that had the highest probability (among such entries) of belonging to the positive class, as well as the converse case.

The selection yielded an initial sample of 131 late-T and Y dwarf candidates. After further visual inspection, we prioritized 32 with either no detection or a marginal detection in $W1$ (hinting at an extremely low temperature) and visible motion (hinting at their proximity). These are being followed-up through our *Spitzer* campaign (see Section 4) to obtain ch1 (3.6 μm) and ch2 (4.5 μm) photometry to confirm/refute their nature and estimate effective temperature and photometric distance. CWISEP J1935-1546 is the reddest among the objects followed-up so far, with $W2 = 15.926 \pm 0.085$ mag, $W1 - W2 = 2.58 \pm 0.37$ mag, and $\text{ch1-ch2} = 3.24 \pm 0.31$ mag (see next section).

4. SPITZER FOLLOW-UP

Spitzer observations were taken as part of program 14034 (Meisner, PI). Seven exposures of 30 s were taken in each band, and these exposures were dithered using a random dither pattern of medium scale. The number of individual exposures was chosen so that we would obtain a 5σ detection at $\text{ch1-ch2} = 2.75$ mag.

Our target is very faint in the ch1 mosaic, and to measure it we had to lower the SNR for detection from 5 (the default value in MOPEX/APEX) down to 2. For the aperture photometry, we used an aperture with a radius of 4 pixels (*aperture1* in the MOPEX output files) and a sky annulus with a 24-to-40-pixels radius. For the PRF-

⁴ <http://byw.tools/wiseview>

Table 1. CatWISE and *Spitzer* photometry for CWISEP J1935–1546.

Band	Magnitude	Notes
CatWISE W1	18.509±0.359	stationary fit (<i>w1mpro</i>)
CatWISE W2	15.926±0.085	stationary fit (<i>w2mpro</i>)
CatWISE W1	18.534±0.396	motion fit (<i>w1mpro_pm</i>)
CatWISE W2	15.852±0.079	motion fit (<i>w2mpro_pm</i>)
<i>Spitzer</i> ch1	19.089±0.262	aperture
<i>Spitzer</i> ch2	15.633±0.018	aperture
<i>Spitzer</i> ch1	18.892±0.314	PRF fit
<i>Spitzer</i> ch2	15.647±0.023	PRF fit

fit photometry, we used a set of warm PRFs built by Jim Ingalls (see Kirkpatrick et al. 2019), which are very similar to the warm mission PRFs developed by Hora et al. (2012), that are available on the IRSA website⁵. For the aperture photometry, the resulting raw fluxes were multiplied by the aperture corrections recommended in Table 4.7 of the IRAC Instrument Handbook – 1.208 for ch1 and 1.221 for ch2 – to obtain the flux in units of μJy ; for PRF-fit photometry, the resulting raw fluxes were divided by the correction factor recommended in Table C.1 of the IRAC Instrument Handbook – 1.021 for ch1 and 1.012 for ch2. These aperture and PRF-fit fluxes were then converted from μJy to magnitudes using the flux zero points in the Handbook’s Table 4.1 (280.9±4.1 Jy in ch1 and 179.7±2.6 Jy in ch2), propagating the uncertainty in zero point and flux into the final measurement error. This final photometry is given in Table 1. The ch1 detection reported here corresponds to a SNR of 3.6.

CWISEP J1935–1546 has ch1–ch2 = 3.24±0.31 mag (PRF; the aperture color is 3.46±0.26), overlapping with WISE J0855–0714 (3.55±0.07 mag), and similar to the second reddest brown dwarf known, WISE J035000.32–565830.2 (3.25±0.10 mag; Kirkpatrick et al. 2012). Figure 1 shows the unWISE *W1* and *W2* coadds, and our *Spitzer* ch1 and ch2 mosaics.

5. ASTROMETRY

The CWISEP J1935–1546 CatWISE measured motion is $\mu_\alpha \cos \delta = 400 \pm 100 \text{ mas yr}^{-1}$, $\mu_\delta = -90 \pm 120 \text{ mas yr}^{-1}$. However, with the aid of our *Spitzer* follow-up observation, we have obtained a better measurement of the target’s motion.

We first re-registered the unWISE epoch coadds to the *Gaia* astrometric frame. We extracted sources from the individual epoch coadds using the CatWISE pipeline.

Because that was run on individual epochs, no “motion fit” was possible, and therefore the positions used are those resulting from the “stationary fit” (see Section 2).

We then selected a sample of bright reference stars to be used for re-registration. We retained only stars with $\sigma_\alpha, \sigma_\delta < 0.1''$, $W1 > 8.1 \text{ mag}$ and $W2 > 6.7 \text{ mag}$ (the saturation limits for *WISE*; Cutri et al. 2012). After these cuts were applied, our initial re-registration set consisted of more than 10,000 stars at each epoch.

We cross-matched our re-registration set to *Gaia* DR2. We used *Gaia* DR2 astrometry to correct the positions of all of the *Gaia* stars in the CatWISE field to the CatWISE epoch in question, and matched them to the re-registration set using a 2.75'' radius (corresponding to one unWISE pixel), retaining only the closest matching *Gaia* source for each re-registration star. We typically found ~ 700 *Gaia* stars at each epoch.

The re-registration stars were used to fit both a 6th order and a 12th order transformation between each epoch coadd and *Gaia* DR2, using our own IDL code. The fit included a 3 σ clipping iteration, removing re-registration stars whose re-registered position after the first fit iteration was off by more than three times the formal errors of the fit from their *Gaia* DR2 position. The use of a 12th order transformation did not significantly reduce the residuals of the fit, and therefore we adopted the 6th order transformation.

To determine reliable uncertainties on the coordinates of CWISEP J1935–1546 at each epoch, we examined the dispersion between the re-registered positions of all stars in the field (without any restriction on their positional accuracy), and their *Gaia* DR2 positions. We found that at $W2 \sim 16 \text{ mag}$ (the brightness of CWISEP J1935–1546) the formal uncertainties reported by WPHOT underestimate by a factor of ~ 1.6 the observed dispersion. We therefore multiply the formal uncertainties by that factor. CatWISE positions and our adopted uncertainties are listed in Table 2.

For the re-registration of the *Spitzer* ch2 mosaic, and the measurement of CWISEP J1935–1546 at that epoch, we adopted the same method described in Kirkpatrick et al. (2019).

Finally, we performed both a linear fit and a 5-parameter astrometric fit (position + proper motion + parallax motion) to the CatWISE and *Spitzer* ch2 positions of CWISEP J1935–1546 as a function of time (listed in Table 2). The target falls below the signal-to-noise-ratio threshold for detection by the CatWISE pipeline (SNR = 1.8) in two of the nine *WISE* plus *NEOWISE* epochs.

The linear fit yielded $\mu_\alpha \cos \delta = 337 \pm 69 \text{ mas yr}^{-1}$, $\mu_\delta = -50 \pm 97 \text{ mas yr}^{-1}$, while the 5-parameter astro-

⁵ See <http://irsa.ipac.caltech.edu/data/SPITZER/docs/irac/calibrationfiles/>.

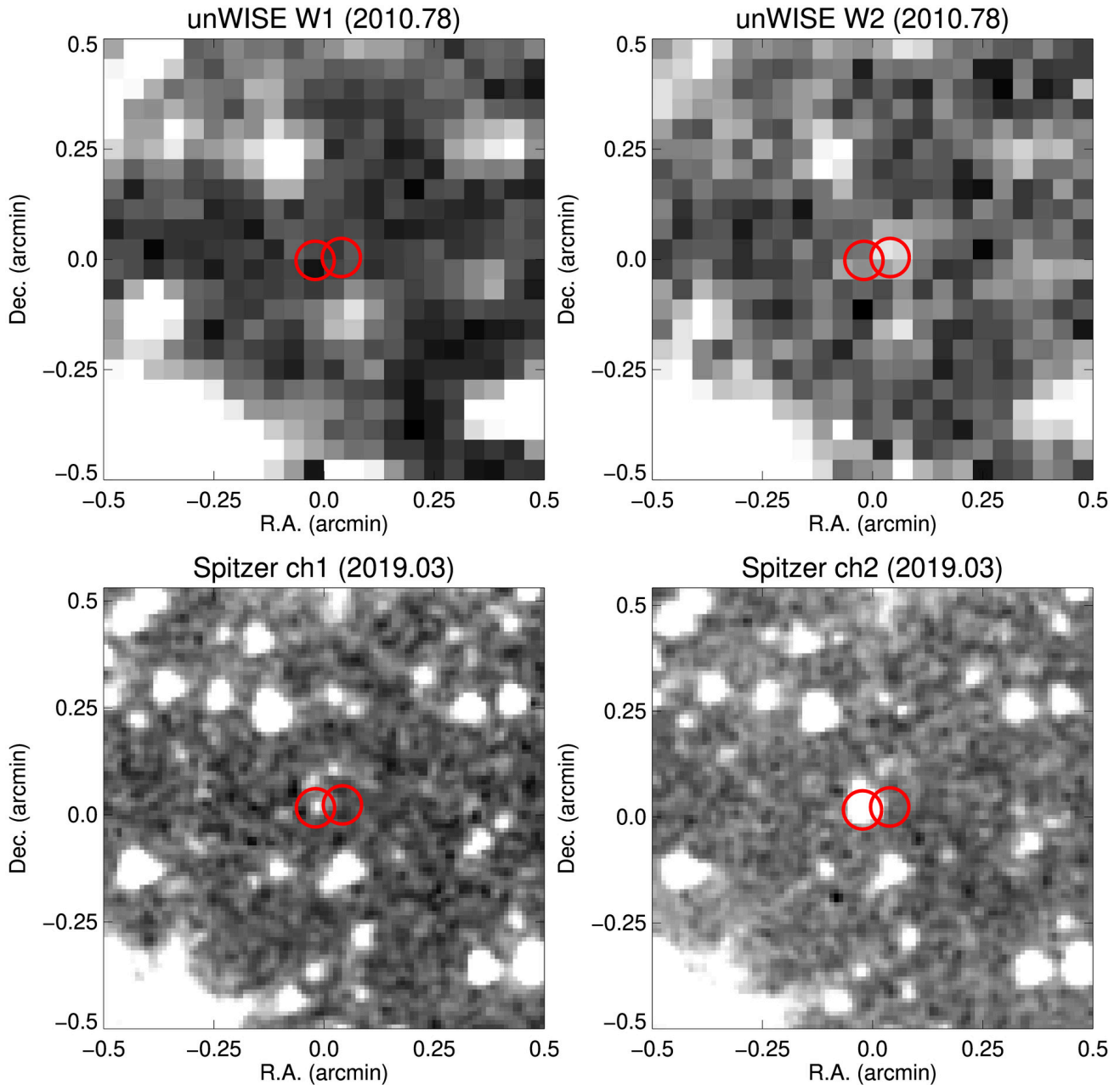


Figure 1. 1×1 arcmin cutouts from the unWISE W1 and W2 epoch coadds (top left and right), and the *Spitzer* ch1 and ch2 mosaic (bottom left and right), centered around CWISEP J1935–1546. Red circles mark its position at the two epochs shown.

metric fit yielded $\mu_\alpha \cos \delta = 341 \pm 90 \text{ mas yr}^{-1}$, $\mu_\delta = -36 \pm 113 \text{ mas yr}^{-1}$, and a trigonometric parallax of $-100 \pm 440 \text{ mas}$. The negative parallax is clearly unphysical and not statistically significant. We therefore adopt the values from the linear fit. The results of the linear fit are presented in Figure 2.

6. ANALYSIS

The ch1–ch2 color for CWISEP J1935–1546 is comparable to that of the coldest brown dwarf known, WISE J0855–0714. In Figure 3 we show T_{eff} as a function of *Spitzer* ch1–ch2 color for a sample of known late-T and Y dwarfs from the literature (see Kirkpatrick et al. 2019, and references therein).

We can use our *Spitzer* photometry and the recent polynomial relations presented in Kirkpatrick et al. (2019) to derive an effective temperature estimate and

Table 2. Measured positions for CWISEP J1935–1546. The 2019 position was obtained through our *Spitzer* follow-up. The target is undetected in two of the nine unWISE epoch coadds.

R.A. (deg)	$\sigma_{\text{R.A.}}$ (arcsec)	Dec. (deg)	$\sigma_{\text{Dec.}}$ (arcsec)	Epoch
293.8267517	0.9	-15.7722349	1.4	2010.2842
293.8270569	1.0	-15.7723198	1.3	2010.7764
293.8275452	1.2	-15.7720318	1.1	2015.2857
293.8275146	1.1	-15.7723351	1.4	2015.7695
293.8275452	1.1	-15.7723131	1.3	2016.7525
293.8276062	1.4	-15.7726307	1.4	2017.2799
293.8276978	1.1	-15.7723455	1.2	2017.7436
293.8277930	0.01	-15.7723462	0.01	2019.0267

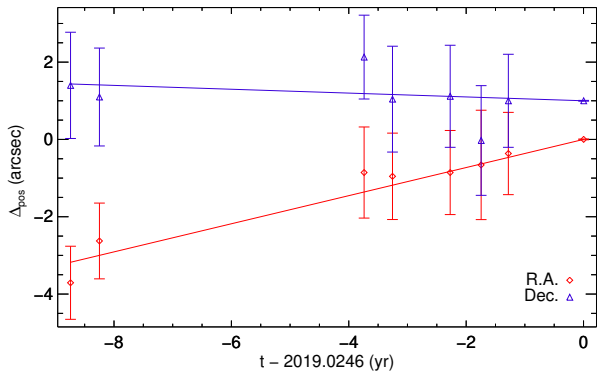


Figure 2. A linear fit to the coordinates of CWISEP J1935–1546 as a function of time. R.A. (red diamonds), Dec. (blue triangles), and time are relative to their variance-weighted mean.

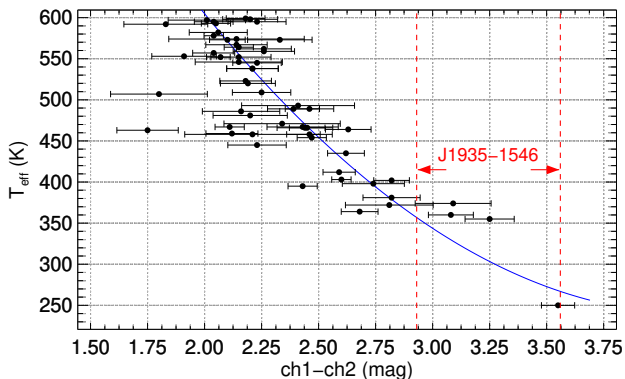


Figure 3. T_{eff} as a function of *Spitzer* ch1–ch2 colors for nearby late-T and Y dwarfs. Black points are objects taken from Kirkpatrick et al. (2019, Table 8). The red dashed lines encompass the 1σ color range for CWISEP J1935–1546. Overplotted in blue is the polynomial relation presented in Kirkpatrick et al. (2019).

photometric distance for CWISEP J1935–1546. Using the ch1–ch2 color to absolute ch2 magnitude relation, we obtain a 1σ distance estimate of 5.6–10.9 pc. Given this estimated distance and the proper motion measured here, CWISEP J19351546 has an estimated tangential velocity in the range 7–22 km s^{-1} , consistent with the tangential velocity distribution for L, T and Y dwarfs in the solar neighborhood from Smart et al. (2019) and Kirkpatrick et al. (2019).

The ch1–ch2 colour to T_{eff} relation from Kirkpatrick et al. (2019) indicates a T_{eff} in the range ~ 270 –360 K, which would make CWISEP J1935–1546 one of the coldest brown dwarfs discovered so far (see Figure 3).

Given the temperature derived above, we can estimate a mass for this object using the BT-Settl models (Allard et al. 2012, 2013). If we assume CWISEP J1935–1546 is a field object, with age in the ~ 500 Myr – 13 Gyr range, it would have a mass in the range 2–20 M_{Jup} . We can narrow down the age and mass range by taking into account the fact that the tangential velocity estimated here is consistent with the population of nearby ultracool dwarfs, whose age is in the range ~ 1.5 –6.5 Gyr (see e.g. Wang et al. 2018, and references therein). In this age range, CWISEP J1935–1546 would have a mass between 3 and 14 M_{Jup} .

No other photometry is currently available for this object, as it is well below the detection threshold for existing optical and near-infrared surveys. The position of CWISEP J1935–1546 is covered by VHS and PanSTARRS, but the target is undetected in both, as well as in the *W3* and *W4* images from AllWISE. Given the T_{eff} and distance ranges estimated above, the expected *H* magnitude would be 23.7–25.1 mag, a depth prohibitive for most ground-based facilities, particularly for spectroscopy. Spectroscopic characterization for this extremely cold object will necessarily have to wait for the launch of *JWST*.

The discovery of CWISEP J1935–1546 starts to bridge the existing gap between known warmer Y dwarfs and the extremely cold WISE J0855–0714. CatWISE, as well as “Backyard Worlds: Planet 9” (a NASA-funded citizen science project; Kuchner et al. 2017) are now fully exploiting the potential of the *WISE* and *NEOWISE* data set to uncover more of these frigid, free-floating planetary mass objects. CWISEP J1935–1546 is part of a larger sample of discoveries by these two highly complementary projects, and joint observing campaigns are now underway to fully characterize this compelling population. By populating this region of parameter space we can not only put strong observational constraints on the mass function for extremely low mass objects,

but also understand the processes that shape such cold, planet-like atmospheres.

This research was partly carried out at the Jet Propulsion Laboratory, California Institute of Technology, under a contract with NASA.

FM is supported by an appointment to the NASA Postdoctoral Program at the Jet Propulsion Laboratory,

administered by Universities Space Research Association under contract with NASA.

AMM acknowledges support from Hubble Fellowship HST-HF2-51415.001-A.

CatWISE is funded by NASA under Proposal No. 16-ADAP16-0077 issued through the Astrophysics Data Analysis Program, and uses data from the NASA-funded WISE and NEOWISE projects.

This work is based in part on observations made with the Spitzer Space Telescope, which is operated by the Jet Propulsion Laboratory, California Institute of Technology under a contract with NASA.

REFERENCES

- Allard, F., Homeier, D., & Freytag, B. 2013, *Mem. Soc. Astron. Italiana*, 84, 1053
- Allard, F., Homeier, D., Freytag, B., & Sharp, C. M. 2012, in *EAS Publications Series*, Vol. 57, EAS Publications Series, ed. C. Reyl , C. Charbonnel, & M. Schultheis, 3–43
- Best, W. M. J., Liu, M. C., Magnier, E. A., et al. 2017, *ApJ*, 837, 95
- Burgess, A. S. M., Moraux, E., Bouvier, J., et al. 2009, *A&A*, 508, 823
- Burrows, A., Marley, M., Hubbard, W. B., et al. 1997, *ApJ*, 491, 856
- Caselden, D., Westin, III, P., Meisner, A., Kuchner, M., & Colin, G. 2018, *WiseView: Visualizing motion and variability of faint WISE sources*, *Astrophysics Source Code Library*, , ascl:1806.004
- Chambers, K. C., Magnier, E. A., Metcalfe, N., et al. 2016, *ArXiv e-prints*, arXiv:1612.05560
- Chen, T., & Guestrin, C. 2016, in *Proceedings of the 22Nd ACM SIGKDD International Conference on Knowledge Discovery and Data Mining*, KDD '16 (New York, NY, USA: ACM), 785–794.
<http://doi.acm.org/10.1145/2939672.2939785>
- Claesen, M., & De Moor, B. 2015, *arXiv e-prints*, arXiv:1502.02127
- Cushing, M. C., Moskovitz, N., & Gustafsson, A. 2018, *Research Notes of the American Astronomical Society*, 2, 50
- Cutri, R. M., Wright, E. L., Conrow, T., et al. 2012, *Explanatory Supplement to the WISE All-Sky Data Release Products*, Tech. rep.
- . 2013, *Explanatory Supplement to the AllWISE Data Release Products*, Tech. rep.
- Faherty, J. K., Gagn , J., Burgasser, A. J., et al. 2018, *ApJ*, 868, 44
- Faherty, J. K., Riedel, A. R., Cruz, K. L., et al. 2016, *ApJS*, 225, 10
- Gaia Collaboration, Brown, A. G. A., Vallenari, A., et al. 2018, *A&A*, 616, A1
- Henry, T. J., Jao, W.-C., Winters, J. G., et al. 2018, *AJ*, 155, 265
- Hora, J. L., Marengo, M., Park, R., et al. 2012, in *Proc. SPIE*, Vol. 8442, *Space Telescopes and Instrumentation 2012: Optical, Infrared, and Millimeter Wave*, 844239
- Kirkpatrick, J. D., Cushing, M. C., Gelino, C. R., et al. 2011, *ApJS*, 197, 19
- Kirkpatrick, J. D., Gelino, C. R., Cushing, M. C., et al. 2012, *ApJ*, 753, 156
- Kirkpatrick, J. D., Schneider, A., Fajardo-Acosta, S., et al. 2014, *ApJ*, 783, 122
- Kirkpatrick, J. D., Martin, E. C., Smart, R. L., et al. 2019, *ApJS*, 240, 19
- Kuchner, M. J., Faherty, J. K., Schneider, A. C., et al. 2017, *ApJL*, 841, L19
- Kuhn, M., & Johnson, K. 2013, *Applied predictive modeling*, Vol. 26 (Springer)
- Lawrence, A., Warren, S. J., Almaini, O., et al. 2007, *MNRAS*, 379, 1599
- Lindgren, L., Hern andez, J., Bombrun, A., et al. 2018, *A&A*, 616, A2
- Luhman, K. L. 2014, *ApJL*, 786, L18
- Mamajek, E. E., Marocco, F., Rees, J. M., et al. 2018, *Research Notes of the American Astronomical Society*, 2, 205
- Marsh, K. A., & Jarrett, T. H. 2012, *PASA*, 29, 269
- Masci, F. 2013, *ICORE: Image Co-addition with Optional Resolution Enhancement*, *Astrophysics Source Code Library*, , ascl:1302.010
- McMahon, R. G., Banerji, M., Gonzalez, E., et al. 2013, *The Messenger*, 154, 35

- Meisner, A. M., Lang, D., & Schlegel, D. J. 2018a, *AJ*, 156, 69
- Meisner, A. M., Lang, D. A., & Schlegel, D. J. 2018b, *Research Notes of the American Astronomical Society*, 2, 202
- Pedregosa, F., Varoquaux, G., Gramfort, A., et al. 2011, *Journal of machine learning research*, 12, 2825
- Sanders, D. B., Salvato, M., Aussel, H., et al. 2007, *ApJS*, 172, 86
- Scholz, R.-D., & Bell, C. P. M. 2018, *Research Notes of the American Astronomical Society*, 2, 33
- Skrutskie, M. F., Cutri, R. M., Stiening, R., et al. 2006, *AJ*, 131, 1163
- Smart, R. L., Marocco, F., Sarro, L. M., et al. 2019, *MNRAS*, arXiv:1902.07571
- Tan, P.-N. 2018, *Introduction to data mining* (Pearson Education India)
- Wang, Y., Smart, R. L., Shao, Z., et al. 2018, *PASP*, 130, 064402
- Wright, E. L., Eisenhardt, P. R. M., Mainzer, A. K., et al. 2010, *AJ*, 140, 1868
- Wright, E. L., Mainzer, A., Kirkpatrick, J. D., et al. 2014, *AJ*, 148, 82
- York, D. G., Adelman, J., Anderson, Jr., J. E., et al. 2000, *AJ*, 120, 1579